7.2 Constitutive, Damage and Plasticity Laws for Candidate Fusion Alloys —

T. Yamamoto and G. R. Odette, Y. Wu (University of California Santa Barbara)

OBJECTIVE

Objectives of this study is to derive true stress-stain constitutive [s(e)] and damage laws, as well as coupled plasticity rules for candidate fusion reactor structural materials, that provide with key elements of a failure evaluation model of fusion reactor structures. For that purpose we need to establish a self-consistent approach to derive [s(e)] beyond the strain range that standard uniaxial tensile tests can probe, especially in irradiated alloys that immediately neck in standard tensile tests.

SUMMARY

Standard uniaxial tensile tests cannot provide generally transferable post-yield information on deformation and ductile failure for materials with low uniform strain limits. Deformation mediated failure is not only controlled by the intrinsic constitutive properties, but also extrinsic factors, especially the loading-specimen geometry. A self-consistent approach is used to derive true stress-stain constitutive [s(e)] laws, for candidate fusion reactor structural materials encompassing a range of unirradiated and irradiated conditions. In this report, unirradiated F82H with 0 to 80% of cold-work and neutron and spallation proton irradiated F82H were evaluated. The approach is based on simultaneous measurements and finite element method (FEM) simulations of engineering stress-strain s(e) curves, that are consistent only for a unique s(e) law. TEM observations of the selected deformed specimens were also performed to obtain microstructural insight. The most important and surprising result is that the s(e) of the irradiated alloys are consistently higher that for unirradiated condition over a wide range of strain. The s(e) after neutron irradiation are higher than in the 80% cold worked unirradiated condition at high strains. For deformation conditions that do not lead to plastic flow instabilities the higher strength levels are an asset even if accompanied by the low initial stain hardening rates following neutron irradiations. Further, there is evidence that high levels of He may suppress the initial loss strain hardening. If verified by additional experiment and modeling, these conclusions will have a tremendous impact on assessing the effects of irradiation service on the failure limits of fusion structures.

PROGRESS AND STATUS

Introduction

Deformation controlled failure of a structure is mediated by the interaction of a number of intrinsic properties, including constitutive properties and plasticity laws, as well as extrinsic factors, such as geometry and loading conditions. Standard techniques, such as the uniaxial tensile test, cannot provide all of the information relevant to predicting deformation and failure, especially for irradiated materials where low ductility limits the strain range that can be probed. Accordingly, we report progress in developing advanced methods to predict local deformation limits for fusion structures in terms of structural stress-strain [s(e)] or load-displacement (P- D) behavior, accounting for both intrinsic and extrinsic factors. The first step requires developing a self-consistent set of constitutive and plasticity laws for materials of interest, both unirradiated and irradiated.

Approach

The approach is to measure P-D or engineering stress-strain [s(e)] curves and characterize and quantify large geometry changes (LGC) and deformation-flow (micro to macro) patterns of strain distributions (SD) for a wide variety of test geometries to access high stains and bound key structural conditions. Examples are shown in Fig.1. The experimental information is combined with finite element modeling (FEM) of the corresponding specimen(s) during testing to simulate LGC behavior, P-D/s(e) and SD. The true-stress/strain constitutive equation s(e) used in the finite element analysis can be varied, and the computed values of P-D/s(e), LGC and SD compared to the measured values. Differences are used to adjust the $\sigma(\varepsilon)$, and the process proceeds iteratively to obtain a maximum self-consistency.

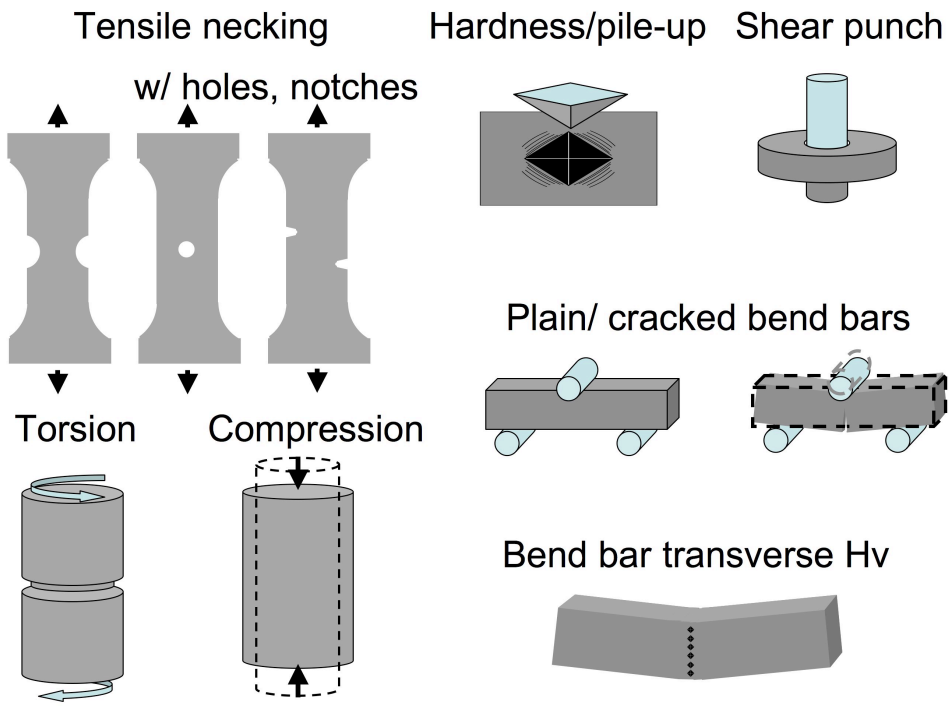

Figure 1. Examples of test techniques that can probe high strain behavior of structural materials coupled with finite element simulations to derive a self-consistent constitutive [s(e)] behavior of the materials.

Experimental Details

The alloy used in the research is a tempered martensitic steel, F82H. The Chemical composition of F82H alloy shown in Table 1. The as-tempered (AT) condition was rolled into two thickness reductions to produce 20% and 80% of cold work (CW), respectively. Miniature flat sheet SS-J2 type tensile specimens shown in Fig. 2 with thickness of 0.5 mm were prepared for those three conditions. The specimens were tested on a MTS load frame at room temperature. Tensile specimens of the same geometry except with a thicker 0.75 mm thickness had been irradiated in HFIR to 7 and 18 dpa at 300 ^{o}C and tested at room temperature. The

results have been reported by Hirose et al. [1]. Tong and Dai reported tensile test results of the same material irradiated in STIP-III (spallation target irradiation program) [2]. The specimen with 5 x 1 x 0.4 (mm) gauge sections were irradiated at 305°C to13 dpa and 995 appm He.

Table 1. Chemical composition of F82H IEA heat.

Cr	W	V	Mn	Ta	Ni	Cu	Ti	Mo	Fe
7.82	1.98	0.19	0.1	0.04	0.02	0.01	0.004	0.0026	Bal.
Nb	Co	Al	Si	S	C	N	B	P	
0.0002	0.0024	0.001	0.07	0.001	0.09	0.007	0.0002	0.003	

Transmission electron microscope (TEM) characterization was performed on the AT and 80% CW conditions both in the undeformed tabs and the highly deformed region near the fracture surface using the focus ion beam (FIB) micro-machining method. Dislocation density was measured using the so-called two-circles method [3].

Finite Element Method Analyses

The finite element (FE) simulations of tensile tests were performed using the ABAQUS 6.9 software package for a three-dimensional mesh, consisting of ≈ 1400 brick elements that, as shown in Fig. 2, models 1/8 of gauge section partially including the end tab. The s(e)data was directly converted to s(e) up to the necking instability strain (or uniform elongation), e_u. The strain hardening ds/de data at $e < e_u$ was fitted to modified Voce-Mecking model based on the competing dislocation dynamics storage with increasing strain and annihilation controlled by the dislocation density, r. As Spatig et. al. has showed [4], the model can be given in terms of the strain hardening, s_{sh} as shown in Eq. (1), based on the dislocation hardening theory, $s_{sh} = Mamb\sqrt{r}$, where M is Taylor factor, a is the strength factor, m is shear modulus and b is Burgers vector.

$$d\sigma/d\varepsilon = P_1/\sigma_{sh} - P_2\sigma_{sh} = P_1/(\sigma_t - \sigma_o) - P_2(\sigma_t - \sigma_o) \quad (1)$$

The fitted P_1, P_2, and s_o were used to extrapolate s(e) up to a steady state saturation at ds/de = 0. The initial s(e) is then iteratively adjusted until the FE engineering s(e) prediction matches the experimental curve.

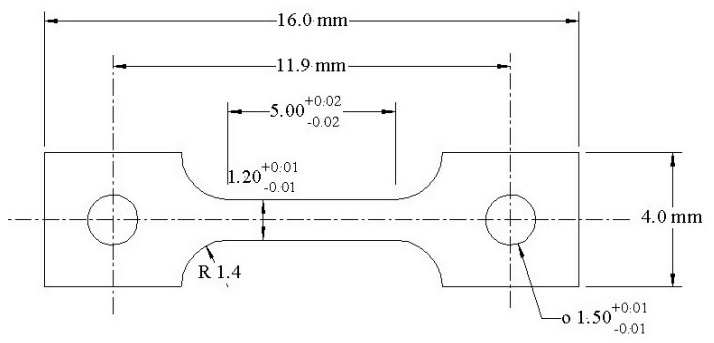

Figure 2. Geometry of SS-J type tensile specimens. SS-J2 with 0.5 mm thickness and SS-J3 with 0.75 mm thickness were used in this research.

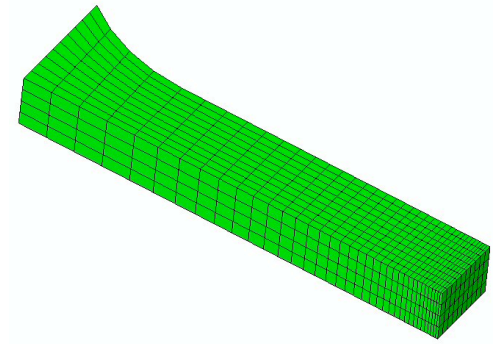

Figure 3. An example of 3D model used in a finite element method simulation of tensile tests

Results and Discussion

Figures 4a-f show the results of iterative FE simulations of F82H IEA tensile stress strain curves for (a) AT, (b) 20% CW, (c) 80% CW, (d) 7 dpa and (e) 18 dpa neutron irradiated and (f) STIP irradiated (13 dpa and 995 appm He) conditions. The green dotted line shows final s(e) model, and the blue solid and red dashed lines show FE simulated and experimental engineering s(e) curves, respectively. In all cases the converged FE simulation is in good agreement with experimental s(e) curve over a wide range of e. As are summarized in Fig. 5, the derived s(e) models vary significantly for the different alloy conditions. The as tempered (AT) alloy s(e) does not saturate up to very high strains and strain hardens rate $d\sigma/de > \approx 300$ MPa reaching $\sigma_{sh,at} \approx 300$ MPa at $e_p \approx 0.8$. The 20% CW condition $\sigma_{sh,20}$ does not saturate up to $e_p \approx 1$, but ds/de continuously decreases at high strains. The 80% CW condition $\sigma_{sh,80}$ saturates almost immediately, at a constant s(e) that is ≈ 400 MPa higher than σ_y in AT condition. The true CW

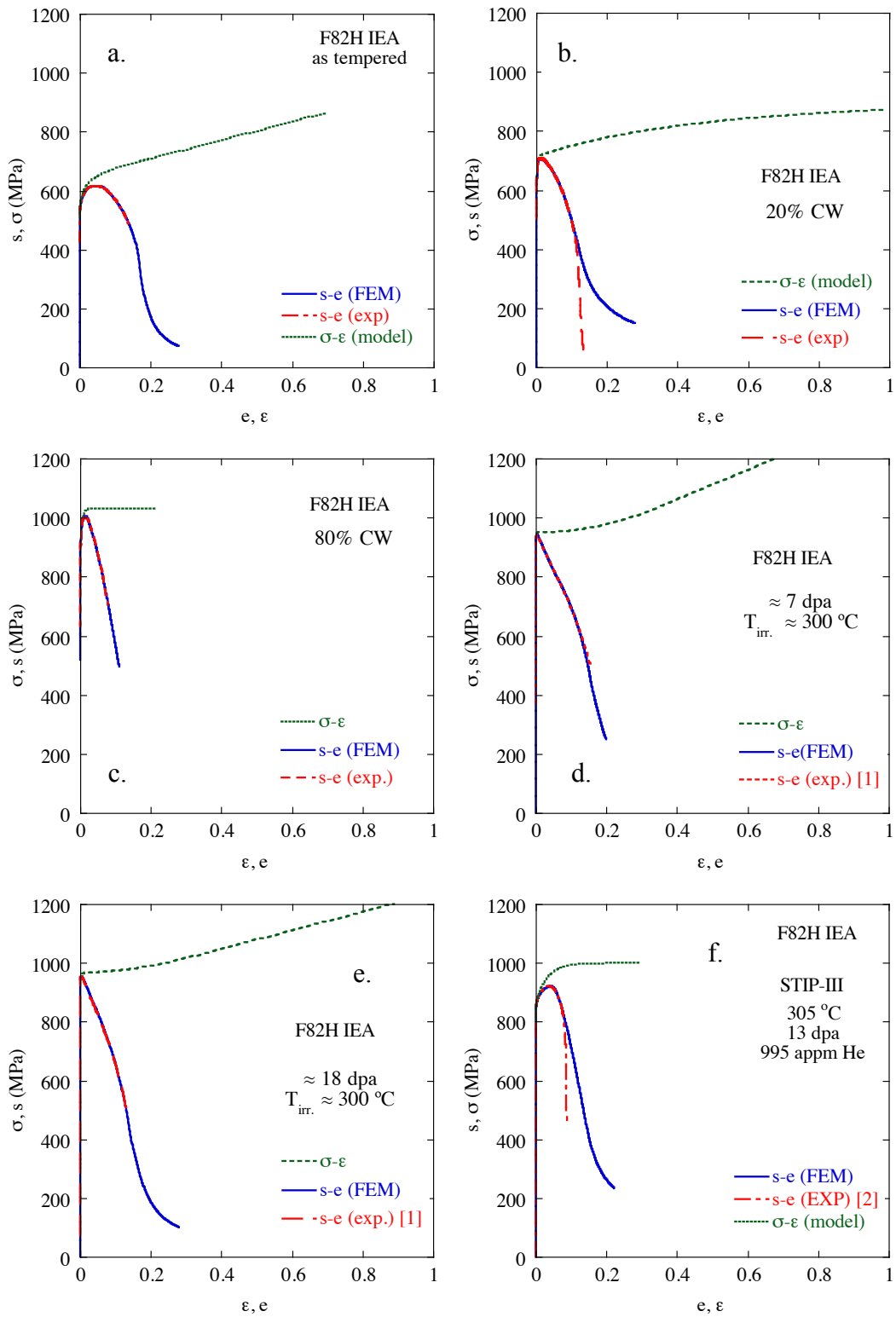

Figure 4. Final s(e) model for FE simulation of tensile s(e) curve in comparison with the experimental s(e) of F82H IEa for (a) AT, (b) 20% CW, (c) 80% CW, (d) 7 dpa and (e) 18 dpa neutron irradiated, and (f) spallation proton irradiated (13 dpa and 995 appm He) conditions.

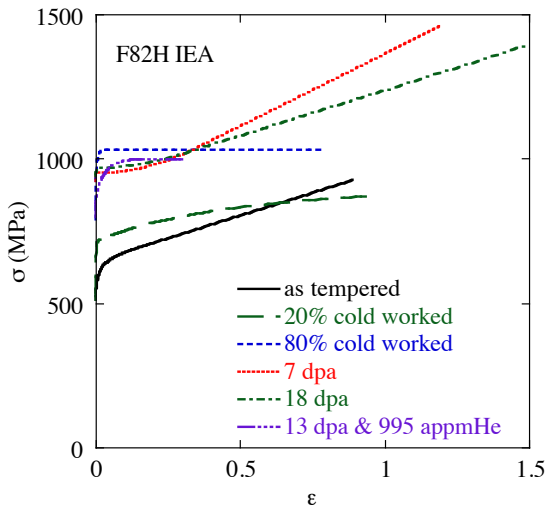

Figure 5. Comparison of model s(e) curves of F82H IEA alloy for various conditions.

Table 2. Dislocation density measured in TEM observation of tested tensile specimens in undeformed end tab and most deformed near fracture surface locations.

	Base	Deformed
As tempered	$6x10^{14}m^{-2}$	$1x10^{15}m^{-2}$
80%CW	$2x10^{15}m^{-2}$	$2x10^{15}m^{-2}$

rolling primary strains are 0.22 and 1.60 of the 20 and 80% CW conditions, respectively. Note the $s_{at}(0.22)$ for the AT condition is approximately equal to the s_y in the CW alloy with the same primary strain. The AT s(0.62) is also similar to the $s_{20}(0.4)$ suggesting that the tensile and CW strains are additive. Assuming a constant ≈ 300 MPa the AT reaches the saturated s_{80} ≈ 1032 MPa at an extrapolated e ≈ 1.34, which is ≈ 0.3 lower than the true primary strain of 80% CW. However, the corresponding ds/de Is much lower in the 20% CW condition, suggesting that much higher e would be needed to reach flow stress saturation in this case, possibly explaining the difference in saturation strain. Table 2 shows the dislocation densities in the AT and 80% CW conditions with no further tensile deformation and at the fracture e ≈ 0.7 in the AT case. Assuming a constant rate of dislocation storage of ≈ $0.6x10^{15}/m^2$ and additional strain of ≈ 1.7 would be needed in the AT condition to yield the saturated density of $2x10^{15}/m^2$ or a total e ≈ 2.4 versus ≈ 1.6 for the 80% CW condition. Thus the saturation dislocation density and s appear to be 1 -2 x $10^{15}/m^2$ and 1030 respectively in the unirradiated F82H.

Both neutron irradiated conditions have low strain hardening up to e ≈ 0.3, resulting in immediate necking. However, at higher e the ds/de is between ≈ 300 and 600 MPa that is equal to or greater than in the AT condition. The analysis suggests that a high rate of ds/de persists at 1200 MPa at between e of 0.7 and 0.9. Thus there appears to be something fundamentally different for neutron irradiation and strain evolved microstructures compared to those created by deformation strains alone. However, in contrast to the neutron case, strain hardening begins immediately in the spallation proton irradiation condition, with high He as well as displacement damage, and rapidly approaches a saturation level similar to that in the AT and 80 CW alloys. If the mechanisms associated with such behavior could be understood it might be possible to design alloys that avoid loss of uniform strain capacity. More generally for deformation conditions that do not lead to plastic instabilities, the higher strength of irradiated alloys is an asset rather than a liability, as seen in Fig. 5.

CONCLUSIONS

The tools used in the work to derived true s(e) laws in as-tempered, cold-worked and irradiated F82H IEA over the wide range of strain are now used routinely in analysis of deformation and fracture phenomena including conditions pertinent to fusion structures. The various trends s(e) behavior are complex and suggest a strong role of microstructure that is alternatively produced by displacement damage (mostly loops), cold work (network dislocation and subgrain structures) and high He irradiations (loops and bubbles). Notably, in many cases associated with stable plastic deformation, the higher strength of irradiated alloys over a wide range of strains should be considered to be an asset rather than a liability.

FUTURE WORK

In addition to a wide range of applications, future research will be directed at understanding the combined interactive effects of processing; irradiation and strain evolved microstructures, with an eye to optimizing alloy and structural performance. Future research will also be focused on a major limitation of these studies to date, by characterizing and modeling deformation induced damage development that leads to fracture of leading candidate fusion alloys.

ACKNOWLEDGEMENTS

This work was supported by the U. S. Department of Energy, Office of Fusion Energy Sciences, under contract DE-FG03-94ER54275.

REFERENCES

1. T. Hirose et al., *J. Nucl. Mater.* **417** (2011) 108. (ICFRM-14)
2. Z. Tong and Y. Dai, J. Nucl. Mater. **398** (2010) 43.
3. B. Hirsch, A. Howie, R. B. Nicholson, D. W. Pashley and M. J. Whelan, Electron Microscopy of Thin Crystals (1965) 423.
4. P. Satig, G. R. Odette, G. E. Lucas, M. Victoria, *J. Nucl. Mater.* **307-311** (2002) 536.